PSO-HRVSO: SEGMENTATION OF RETINAL VESSELS THROUGH HOMOMORPHIC FILTERING ENHANCED BY PSO OPTIMIZATION

Niladri Halder[1*], Dibyendu Roy[2], Partha Pratim Sarkar[2], Sankar Narayan Patra[1], Subhankar Bandyopadhyay[1]

[1*]Instrumentation and Electronics Engineering, Jadavpur University, Saltlake Campus, Kolkata, 700098, West Bengal, India
[2]Electronics and Communication Engineering, UIT, Burdwan University, Golapbag, Burdwan, 713104, West Bengal, India

ABSTRACT

The structure of retinal blood vessels is crucial for the early detection of diabetic retinopathy, a leading cause of blindness worldwide. Yet, accurately segmenting retinal vessels poses significant challenges due to the low contrast and noise present in capillaries.The automated segmentation of retinal blood vessels significantly enhances Computer-Aided Diagnosis for diverse ophthalmic and cardiovascular conditions. It is imperative to develop a method capable of segmenting both thin and thick retinal vessels to facilitate medical analysis and disease diagnosis effectively. This article introduces a novel methodology for robust vessel segmentation, addressing prevalent challenges identified in existing literature.

The methodology PSO-HRVSO comprises three key stages: pre-processing, main processing, and post-processing. In the initial stage, filters are employed for image smoothing and enhancement, leveraging PSO optimization. The main processing phase is bifurcated into two configurations. Initially, thick vessels are segmented utilizing an optimized top-hat approach, homo-morphic filtering, and median filter. Subsequently, the second configuration targets thin vessel segmentation, employing the optimized top-hat method, homomorphic filtering, and matched filter. Lastly, morphological image operations are conducted during the post-processing stage.

The PSO-HRVSO method underwent evaluation using two publicly accessible databases (DRIVE and STARE), measuring performance across three key metrics: specificity, sensitivity, and accuracy. Analysis of the outcomes revealed averages of 0.9891, 0.8577, and 0.0.9852 for the DRIVE dataset, and 0.9868, 0.8576, and 0.9831 for the STARE dataset, respectively.

The PSO-HRVSO technique yields numerical results that demonstrate competitive average values when compared to current methods. Moreover, it sur-passes all leading unsupervised methods in terms of specificity and accuracy. Additionally, it outperforms the majority of state-of-the-art supervised methods without incurring the computational costs associated with such algorithms. Detailed visual analysis reveals that the PSO-HRVSO approach enables a more precise segmentation of thin vessels compared to alternative procedures.

KEYWORDS

Optimization using PSO, Segmentation of retinal blood vessels, Optimized Top-hat transformation, Homomorphic Filtering.

1. INTRODUCTION

The examination of the eye fundus is extensively utilized by ophthalmologists and other medical practitioners as a standard clinical procedure for preventing, diagnosing, and monitoring the treatment of various ocular conditions including retinal thrombosis, glaucoma, and senile maculopathy, among others [1]. This examination involves a color imaging method of the retinal surface of the human eye, enabling the observation of key anatomical features such as the optic disc, macula, and vascular tree [66].

The segmentation of the retinal vascular tree holds significant importance in the realm of medical imaging because the retina offers a unique avenue to observe blood microcirculation non-invasively, allowing for the detection of various systemic diseases such as hypertension, diabetes, arteriosclerosis, and liver diseases, among others [3,4,6]. By delineating the retinal vessels, valuable morphological data including size, length, width, branching patterns, and angles of the retinal vasculature can be quantified [5]. However, manually performing this segmentation is a laborious process that demands expertise and experience from medical professionals [2]. Moreover, inconsistencies may arise due to subjective interpretations, as experts might employ different criteria for pixel classification [9–11].

Hence, it is imperative to advance and implement automated techniques for robust vessel extraction in Computer-Aided Diagnosis to facilitate early detection and assessment of disorders, aiming to mitigate medical expenses and enhance efficiency [8,7]. Nonetheless, segmentation encounters numerous hurdles. The foremost challenge emanates from the presence of various optical components in the eye fundus, including the optic disk, macula, and artifacts generated by pathologies, impeding the automated segmentation of vessels. The second challenge stems from the variability in vessel width and the subdued contrast of thin vessels against the background. Lastly, the third challenge arises from the diversity in shape, size, and intensity of vessel pixels, complicating accurate segmentation [3,16,14].

In recent decades, numerous techniques have emerged for automatically segmenting retinal vessels using fundus examination, garnering considerable attention from the scientific community due to their increasingly accurate outcomes [13]. These methods are typically categorized as supervised or unsupervised. Supervised methods involve training a classifier with a dataset (training set) to differentiate between vessel and non-vessel pixels, further classified into machine learning and deep learning algorithms. Machine learning approaches typically involve feature extraction, selection, and classification stages, with various feature extractors and classifiers PSO-HRVSO for medical image classification, including bag-of-visual-words, Gaussian filter, and Gabor filter, along with classifiers like K-Nearest Neighbors (K-NN), Random Forest, Support Vector Machine (SVM), and Artificial Neural Networks (ANN) [12–31].

Deep learning techniques offer an advantage over traditional methods by automatically extracting features from raw data, eliminating the need for handcrafted features [34,32]. While supervised methods yield satisfactory results for healthy retinal vessel extraction, a notable limitation is the necessity for ground-truth images, which can be challenging to obtain. Additionally, both machine learning and deep learning algorithms demand time-consuming and computationally expensive training processes to effectively handle new sets of images [9].

Conversely, unsupervised methods in medical image processing involve image segmentation without relying on a training dataset. These approaches utilize various image processing techniques. Initially, the image undergoes enhancement procedures, typically employing morphological operations [33], matched filter responses [39], the complex continuous wavelet transform [37], adaptive histogram equalization [35], Hessian-based filters [36, 38, 44], among others. Sub-

sequently, segmentation occurs through multilevel thresholding [40–43, 48] or region-oriented techniques such as region growing [45, 49] or active contours [46, 47]. These conventional unsupervised methods heavily rely on manual feature extraction for image element representation and segmentation. Generally, supervised methods exhibit higher efficiency and yield superior results [8]. However, unsupervised systems possess a significant advantage in performing vessel segmentation without prior knowledge of ground-truth labels, particularly beneficial for datasets lacking pixel-level labeling information [16]. Additionally, unsupervised methods offer computational efficiency and faster results. Recent research has utilized both supervised and unsupervised methodologies, demonstrating promising performance in retinal vessel segmentation. Nevertheless, the challenge of accurately segmenting thin vessels remains a significant hurdle for optimal performance in existing literature. Thin vasculature offers crucial information for detecting neovascular diseases [14], underscoring the importance of achieving improved vessel segmentation for enhanced detection and diagnosis of eye diseases [64].

This article presents a novel methodology aimed at accurately segmenting retinal vasculature to tackle prevalent challenges encountered in retinal vessel segmentation from eye fundus images. The PSO-HRVSO approach comprises three distinct phases: pre-processing, main processing, and post-processing. During the initial phase, a Gaussian filter is employed to yield a smoothed gray-scale fundus image, followed by PSO optimized image enhancement for obtaining an optimized enhanced fundus image. The main processing phase entails two configurations: the first configuration targets thick vessel segmentation through a combination of filters (Optimized top-hat, Homomorphic, and Median), whereas the second configuration focuses on thin vessel segmentation using a similar combination of filters (Optimized top-hat, Homomorphic, and Matched). Subsequently, morphological image processing is applied during the post-processing phase. Extensive experiments are conducted on two publicly available databases, DRIVE (51) and STARE (50), to evaluate the methodology's performance. The results of performance metrics underscore the method's advantages, demonstrating comparable or superior values in contrast to many contemporary techniques, which often entail higher computational complexity for retinal vessel segmentation.

The major contributions of this article can be outlined as follows:

- Introducing a novel methodology for segmenting thin and thick retinal blood vessels.
- Presenting a new variant of the classical top-hat operation termed as the optimized top-hat.
- Investigating the variation of parameters in the optimized top-hat filter and the homomorphic filter based on the vessel thickness.
- Developing an automated method for robust retinal vessel segmentation suitable for Computer Aided Diagnosing tools.
- Achieving a minimal false positive rate through this PSO-HRVSO method.
- Demonstrating superior specificity and accuracy compared to recent unsupervised methods and competitive performance with supervised methods, while maintaining low computational costs.

2. LITERATURE REVIEW

In the preceding section, numerous relevant papers in contemporary research focus on retinal vascular tree segmentation within fundus images, broadly categorized as supervised and unsupervised methods. Noteworthy advancements in retinal vessel segmentation are briefly outlined below, serving as benchmarks against which the PSO-HRVSO methodology is evaluated.

Recent unsupervised methodologies, such as those introduced by Wang et al. [85] in 2019, involved modifications to top-hat and bottom-hat transformations aimed at enhancing images by mitigating disturbances and noise. Their segmentation approach utilized a novel technique known as flattening of minimum circumscribed ellipse to identify vessels. Similarly, Diaz et al. [84] in the same year PSO-HRVSO employing the Lateral Inhibition technique (LI) to enhance contrast between fundus and retinal vessels. They employed the minimization of cross-entropy via the differential evolution (DE) algorithm for vessel segmentation, optimizing for efficient segmentation.

In 2020, Shukla et al. [89] introduced a fractional filter to eliminate artifacts and noise while preserving thin vessel edges. Their method involved extracting central line pixels using a proprietary algorithm and applying Principal Component Analysis (PCA) to assess eigenvalue maps, followed by region growing operations and localized thresholding for vessel segmentation. Likewise, Dos Santos et al. [88] in the same year utilized Contrast Limited Adaptive Histogram Equalization (CLAHE) and the Wiener filter to enhance image contrast and reduce noise. An Artificial Neural Network (ANN) was employed to optimize filter parameters for optimal results.

Furthermore, Zhou et al. [87] PSO-HRVSO an enhanced line detector followed by Hidden Markov Model (HMM) application for detecting thin vessel lines effectively. Finally, Pachade et al. [90] recommended a novel segmentation configuration involving contrast enhancement, 2D median linear filtering, morphological operations, background estimation, and iterative thresholding to achieve segmentation completeness.

On the contrary, recent developments in supervised methodologies are outlined. In 2019, Adapa et al. [74] introduced a supervised technique involving initial image preprocessing. This involved enhancing the image using a CLAHE filter to improve local contrast, followed by a top-hat transform. Subsequently, feature extraction utilized Zernike moments for binary classification through an Artificial Neural Network (ANN). Similarly, Yang et al. [71] employed the K-Singular Value Decomposition (K-SVD) to derive multiple complementary features using six distinct enhancement algorithms. However, their PSO-HRVSO method required manually annotated ground-truth data for training, essential for vessel classification into thin or thick vessels using the K-SVD algorithm for vessel segmentation dictionary training. Jin et al. [72] introduced the Deformable U-Net (DUNet) for segmentation, a hybrid of the traditional U-Net and Deformable Convolutional Network (Deformable-ConvNet). In 2020, Cheng et al. [73] PSO-HRVSO a novel U-Net architecture specifically tailored for retinal vessel segmentation, enhancing accuracy for vessels of various thicknesses by incorporating a dense block into the network configuration. Lastly, Wu et al. [75] introduced NFN+, a novel configuration comprising two cascading backbones connected by inter-network skip connections. The initial network processes image patches to generate probability maps of primary vessels, while the subsequent network refines these maps to produce segmented results. Supervised approaches entail learning from a model to predict pixel categorization, demonstrating superior performance compared to unsupervised methods. However, certain unsupervised models, including those highlighted here and those PSO-HRVSO in this study, achieve comparable or even superior results with reduced computational overhead and time constraints.

3. METHODOLOGY

This section provides a concise overview of the PSO-HRVSO algorithm, as illustrated in the flowchart depicted in Figure 1. Key concepts integral to the PSO-HRVSO methodology are outlined herein. Notably, the eye fundus image exhibits both thick and thin blood vessels, with the latter often overlooked by previous algorithms. The primary objective of this approach is to effec-

tively segment thick and thin vessels, resulting in two distinct images. These images are subsequently merged to produce a final segmentation outcome.

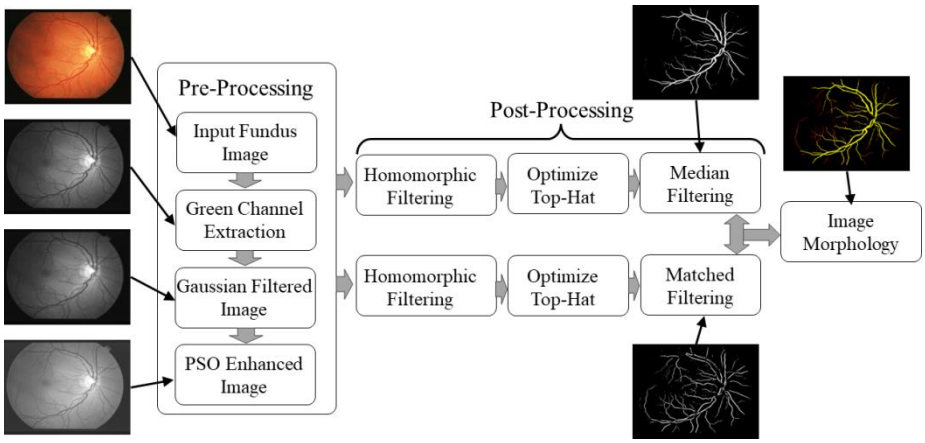

Figure 1:PSO-HRVSO method of vessels segmentation

3.1. Pre-processing

Prior to executing the thick and thin vessels processing phases, it is crucial to implement a pre-processing stage on a retinal eye fundus image, which significantly enhances the outcomes. This pre-processing task encompasses three stages: extracting the green channel of the image, employing a two-dimensional Gaussian filter, and enhancing it through PSO optimization.

3.1.1. Green Component Extraction

The input eye fundus image is presented in RGB format, indicating it's a 24-bit image, with each channel (red, green, and blue) comprising 8 bits. Consequently, the input can be viewed as a three-layered image, and its representation is as follows:

$$I_{Input} = [I_{Red} + I_{Green} + I_{Blue}] \quad (1)$$

The RGB input image, denoted as I_{Input}, consists of three channels: red (I_{Red}), green (I_{Green}), and blue (I_{Blue}). Each channel is represented by its respective layers. Upon analyzing individual channels, the green channel (I_{Green}) exhibits a significant contrast between vessels and the background. In contrast, the red (I_{Red}) and blue (I_{Blue}) channels display higher levels of noise and comparatively lower contrast [56]. Moreover, human visual perception is more responsive to the green channel compared to both red and blue channels [54]. Consequently, the green channel (I_{Green}) is extracted as a grayscale image for further processing.

3.1.2. Gaussian Filtering

While the green-channel of the eye fundus image exhibits commendable vessel-background contrast compared to the RGB input image, incorporating a noise removal step prior to subsequent stages yields positive and productive outcomes. The utilization of Gaussian smoothing filtering algorithm proves advantageous for enhancing image structures, including previously contrasted elements. This filtering technique operates by employing a Gaussian function, rooted in the normal distribution widely utilized in statistics, to compute the transformation applied to each pixel within the two-dimensional set. The Gaussian filtering representation $G(x, y)$ of an image is obtained through the convolution of the input image $I_{Green}(x, y)$ and the two-dimensional Gaussian kernel $g(x, y)$, the mathematical representation as follows:

$$g(x,y) = \frac{1}{2\pi\sigma^2} exp\left(-\frac{x^2+y^2}{2\sigma^2}\right) \quad (2)$$

The parameter σ represents the standard deviation within the Gaussian distribution, governing the extent or breadth of the filter's dispersion. Then the Gaussian distribution can be found from the equation 3.

$$G(x,y) = g(x,y) * I_{Green}(x,y) \quad (3)$$

In the event that the variance value approaches zero, the filter demonstrates an impulse function response, as articulated in Equation 4.

$$G(x,y) = I_{Green}(x,y) \quad (4)$$

With increasing σ^2, the filter's smoothing effect becomes more pronounced. Within this filter, image details significantly smaller than the standard deviation are entirely eliminated. Following various experiments, the variance is determined to be 0.472. The outcome of the pre-processing stage is depicted in Figure 2c.

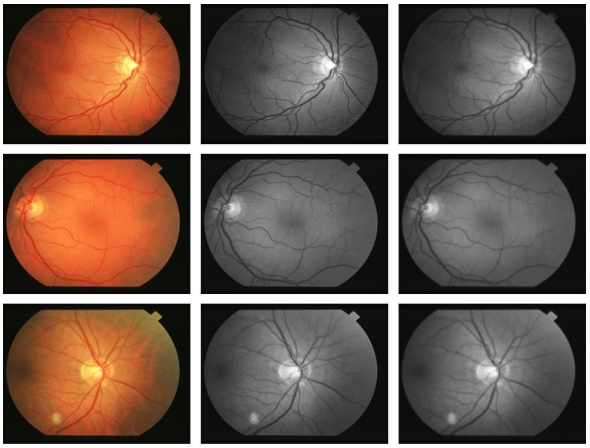

Figure 2: Shows the Gaussian Distributed results (a) Input RGB, (b) Green Component, (c) Gaussian Distribution

3.1.3. PSO Optimization

Particle swarm optimization (PSO) stands out as a widely recognized population-based optimization technique rooted in the principles of swarm intelligence. It leverages the collective behavior of a swarm to efficiently explore a designated search space in pursuit of the optimal solution. PSO operates by employing dynamic entities called "particles" that continually adjust their positions and velocities in a stochastic manner. These adjustments are directed both towards the most promising positions discovered by individual particles and across the entire search space. In a D-dimensional search space, with a swarm size denoted as X, each particle's position is represented as $P_i(p_{i_1}, p_{i_2}, p_{i_3}, \dots\dots\dots\dots, p_{i_D})$, offering a feasible solution to the optimization problem at hand. Correspondingly, the velocity of each particle is characterized by $U_i(u_{i_1}, u_{i_2}, u_{i_3}, \dots\dots\dots\dots, u_{i_D})$.The best previous position for each particle is denoted as $Q_i(q_{i_1}, q_{i_2}, q_{i_3}, \dots\dots\dots\dots, q_{i_D})$, while the overall best position identified by the entire swarm is represented as $Q_g(q_{g_1}, q_{g_2}, q_{g_3}, \dots\dots\dots\dots, q_{g_D})$. These equations, as cited in [53, 52, 55], govern the behaviour of the particles within the PSO framework.

$$u_{i_d}^{k+1} = \omega^k * u_{i_d}^k + a_1 * rand() * \left(q_{i_d} - p_{i_d}^k\right)\Delta t + a_2 * rand() * \left(q_{g_d} - p_{i_d}^k\right)/\Delta t \quad (5)$$

$$p_{i_d}^{k+1} = p_{i_d}^k + \Delta t * u_{i_d}^k \quad (6)$$

$$\omega^k = \omega_{max} - k * (\omega_{max} - \omega_{min})/k_{max}$$

The acceleration coefficients, identified as a_1 and a_2, and the inertia weight, represented by w where w_{max} and w_{min} denote the maximum and minimum values of w, are utilized within a random function $rand()$ adhering to a uniform distribution. The updated value and the maximum number of iterations are denoted by $u_{i_d}^{k+1}$ and $p_{i_d}^{k+1}$ respectively, where $d \in [1,\ D]$. The unit time is commonly denoted as Δt, and the conditions governing the restrictions on $u_{i_d}^{k+1}$ and $p_{i_d}^{k+1}$ are outlined as follows:

$$u_{i_d}^{k+1} = \begin{cases} u_{i_d}^{k+1} & -u_{max} \le u_{i_d}^{k+1} \le u_{max} \\ u_{max} & u_{i_d}^{k+1} > u_{max} \\ -u_{max} & u_{i_d}^{k+1} < -u_{max} \end{cases} \quad (7)$$

$$p_{i_d}^{k+1} = \begin{cases} p_{i_d}^{k+1} & -p_{max} \le p_{i_d}^{k+1} \le p_{max} \\ p_{init} & p_{i_d}^{k+1} > p_{max} \\ p_{init} & p_{i_d}^{k+1} < p_{min} \end{cases} \quad (8)$$

$$p_{init}^{k+1} = p_{min} + rand() * (p_{max} - p_{min}) \quad (9)$$

The term u_{max} denotes the peak value of u while p_{max} and p_{min} signify the upper and lower limits of p, respectively. Presented below is a concise overview of the fundamental stages engaged in the processing of PSO and figure 3 depict the outputs of PSO optimization with a swarm size of 28 and 100 iteration:

1. Commence by establishing the parameters of the Particle Swarm Optimization (PSO) framework, which encompass the maximum and minimum iteration weights, cognitive and social acceleration coefficients, population size, local window size, and the maximum iteration limit.
2. Select an RGB Fundus image as input and subsequently transform it into its green component.
3. Initialize the particles by defining their initial positions and velocities.
4. Evaluate the fitness values for the initialized particles.
5. Identify the optimal individual position for each particle within the swarm.
6. Employ equations 1, 2, and 3 to adjust the positions and velocities of the particles.
7. Update the best individual position for each particle and determine the best group position for the entire swarm.
8. Assess whether the maximum iteration limit has been reached. A. If the limit has been reached, output the particle with the highest HIS value. B. If not, return to step 6 and iterate the process.
9. Conclude the optimization process.

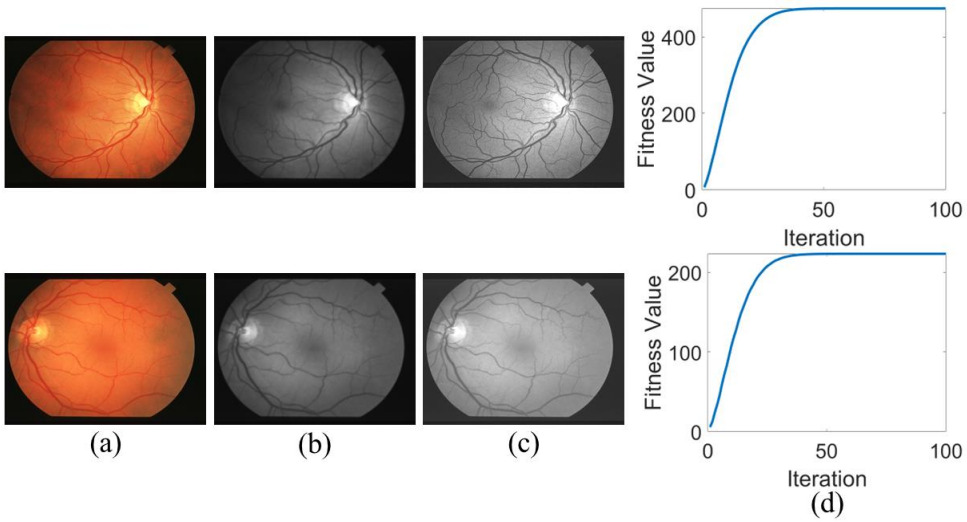

Figure 3: PSO Optimization: (a) RGB Image, (b) Gaussian Distribution, (c) PSO Enhanced, (d) Fitness Curve

3.2. Thick Vessels Segmentation

As illustrated in Figure 1, the thick vessel segmentation procedure comprises three distinct stages, which will be elaborated upon subsequently.

3.2.1. Optimized Top-Hat Algorithm

Morphological image operations serve as a robust tool for image manipulation. Mathematical morphology encompasses algebraic arithmetic operators that are employed on a grayscale 2-D eye fundus image. The top-hat morphological operation entails the disparity between the original image and its morphologically closed-form. This operation elucidates the interplay between the image and a structuring element characterized by specific size and shape [59]. It is utilized to amplify bright objects of interest set against a dark background, such as prominent blood vessels discerned from an image complement (a concept clarified later) of the green channel image where the background transitions to darkness. Denoting a grayscale 2-D image as I_{Input} and the structuring element as SE, the top-hat operation is defined by the following equation:

$$I_{Top\_Hat} = I_{Input} - \left(I_{Input} \circledcirc SE_O\right) \tag{10}$$

Various adaptations of the modified top-hat approach were introduced by Salembier et al. [57]. Mendonça et al. [58] and Bahadar Khan et al. [63] have previously applied these variations to blood vessel segmentation. This study proposes a novel optimized top-hat technique aimed at addressing certain issues identified in the conventional top-hat operation, as discussed in the aforementioned literature. One limitation is the failure to detect minor intensity fluctuations, which are crucial for identifying slender vessels. In this PSO-HRVSO method, the top-hat operator is first applied to a complementary image, and subsequently, morphological image operations are inverted. The PSO-HRVSO optimized top-hat can be described as follows:

$$I_{Optimized\_TH} = I^C_{Input} - \left(I^C_{Input} \circledcirc SE_O\right) \odot SE_C \tag{11}$$

SE_O and SE_E represent the structuring elements utilized for opening ⊙ and closing ⊙ operators correspondingly, while I^C_{Input} denotes the image complement of I_{Input}, delineated as follows:

$$I^C_{Input} = \frac{U}{I_{Input}} \tag{12}$$

The universe U represents all possible values that each pixel can assume. Subsequently, the operation defining the complement of an image is established as follows:

$$I^C_{Input}(x, y) = max(U) - I_{Input}(x, y) \tag{13}$$

The enhancement process for thick vessels utilizes a disk-shaped structuring element for both opening ⊙ and closing ⊙ operations, employing a radius of eight pixels for opening and sixteen pixels for closing.

Figure 4dand 4e illustrate the outcome of employing the PSO-HRVSO optimized top-hat filter and binarized top hat respectively on the input fundus image depicted in Figure 3a whereas figure 4b and 4c illustrate the outcome of employing global top-hat optimization and its binary part. Both Figure 4b and Figure 4d were generated using a structuring element of the same shape and size for both opening and closing operations (a disk with a radius of 10 pixels). A qualitative examination of the images reveals that the PSO-HRVSO optimized top-hat filter significantly improves the contrast of the vessels compared to the classical top-hat filter, enhancing both thick and thin vessels.

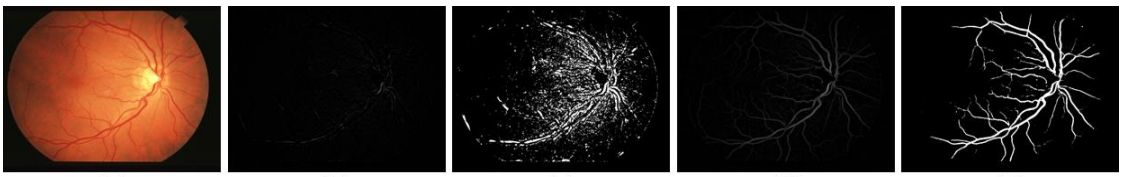

Figure 4: Optimized Top-Hat: (a) Input RGB, (b) Conventional Top-Hat, (c) Binary of (b), (d) Optimized Top-Hat, (e) Binary of (d).

3.2.2. Homomorphic Filtering

If we view it through the lens of the classical intensity model for digital images, an image can be seen as the outcome of light reflected from a scene, subsequently captured by a camera to create the image. Typically, this model is described in relation to the spatial distributions of intensity [60] within a two-dimensional function (such as an image represented by $I_{fundus}(x, y)$), and it is typically depicted as:

$$I_{fundus}(x, y) = l_{fundus}(x, y) r_{fundus}(x, y) \tag{14}$$

In this context, $l_{fundus}(x, y)$ denotes the brightness of the illumination, while $r_{fundus}(x, y)$ delineates the spatial spread of the reflectance, which is formed and influenced by the inherent characteristics of the object and the surrounding environment.

Homomorphic filtering operates in the frequency domain, enabling the adjustment of both illumination and reflectance intensities across the spectral range of an image. This capability facilitates diverse analyses through the application of multiple frequency-domain filters. Typically, the re-

flectance component, $r_{fundus}(x,y)$, spans the entire frequency spectrum, while the illumination component's intensity $l_{fundus}(x,y)$, exhibits gradual changes characterized by low spatial frequencies. Consequently, the illumination component is often centralized within the 2D-Fourier frequency domain. A common challenge in vessel segmentation involves enhancing the reflectance from the fundus image while minimizing the influence of the illumination component's intensity. To address this, a linear frequency-domain filter is employed to attenuate low-frequency components and enhance high-frequency intensities.

The natural logarithm serves as a mathematical tool that transforms multiplication into addition. By applying this principle to Equation 14, we derive the subsequent equation:

$$z_{fundus}(x,y) = ln\left(I_{fundus}(x,y)\right) = ln\left(l_{fundus}(x,y)r_{fundus}(x,y)\right) = ln\left(l_{fundus}(x,y)\right) + ln\left(r_{fundus}(x,y)\right) \quad (15)$$

The logarithm functions as a homomorphism, thus named the filtering process, which translates from a multiplicative number group to an additive number group. This transition enables the application of linear filtering processes. Equation 15 undergoes Fourier transformation, a step that isn't directly feasible due to the inseparability of function multiplication in the Fourier domain.

$$Fn\left[z_{fundus}(x,y)\right] = Fn_z(u,v) + Fn_r(u,v) \quad (16)$$

Filtering is achieved through the multiplication of the image $Fn_z(u,v)$ by a frequency-domain filter $H_{fn}(u,v)$. Among various transfer functions experimented with, the Gaussian high-pass response proves particularly effective for eye fundus images, as represented in Equation 17 in the frequency domain.

$$H_{fn}(u,v) = 1 - exp\left(\frac{-D^2(u,v)}{2\sigma^2}\right) \quad (17)$$

Where $D(u,v) = \sqrt{u^2+v^2}$ and σ represents the measure of the dispersion of the Gaussian curve. The greater the value of σ, the higher the cut-off frequency and the gentler the filtering effect. Upon implementing the filter, we derive the following equation:

$$G_{fn}(u,v) = Fn_z(u,v)H_{fn}(u,v) = Fn_l(u,v)H_{fn}(u,v) + Fn_r(u,v)H_{fn}(u,v) \quad (18)$$

The filtered spectrum of the processed signal is restored by applying a subsequent inverse Fourier transformation in the following manner:

$$Fn^{-1}\left[G_{fn}(u,v)\right] = Fn^{-1}\left[Fn_l(u,v)H_{fn}(u,v)\right] + Fn^{-1}\left[Fn_r(u,v)H_{fn}(u,v)\right] \quad (19)$$

$$g_{fundus}(x,y) = l'_{fundus}(x,y) + r'_{fundus}(x,y) \quad (20)$$

Ultimately, the filtered image, denoted as $l'_{fundus}(x,y)$, undergoes an exponential transformation to reverse the effects of the logarithmic transformation. Equation 21 encapsulates the formulation of this final step in the process.

$$I'_{fundus}(x,y) = exp\left[g_{fundus}(x,y)\right] = exp\left[l'_{fundus}(x,y)\right]exp\left[r'_{fundus}(x,y)\right] \quad (21)$$

Although the illumination and reflectance components aren't completely distinguished in the spectral domain, the homomorphic approach remains a valuable tool that produces significantly

enhanced images [61]. In this scenario, a sigma (σ) value of two is employed to amplify thick vessels, which have considerably higher reflectance values compared to thin vessels.

3.2.3. Median Filtering

Prior to the final operation, salt and pepper noise, induced by a low value of σ during the homomorphic filtering procedure, is eliminated using a median filter. It is noteworthy that the median filter is adept at retaining edges while eliminating noise. It possesses the capability to differentiate between isolated noise and intrinsic features of the input image, such as sharp edges and other details. This capability pertains to high spatial frequencies, thereby preserving previously enhanced thick vessels. The median filter operates by substituting each pixel in the image with the median intensity value within a designated neighborhood $R_n(m,n)$. Mathematically, the resultant image $I'_{median}(x,y)$ after the median filtering process of an image $I_{input}(x,y)$ can be expressed as:

$$I'_{median}(x,y) = M_e\big(I_{input}(m,n), (m,n) \in R\big) \tag{22}$$

The median value of pixels within the region $R_n(m,n)$ is denoted as M_e. Although the noise generated in earlier stages is minimal, it significantly impacts the outcome. The neighborhood size is represented by a matrix of dimensions [2, 2].

Recently, the optimized top-hat method has been reintroduced to enhance the profile of thick vessels, effectively filling small black pixel regions within them. In this instance, the dimensions of the disk-shaped structuring element are notably increased compared to the previous optimized top-hat approach. Operations involving both opening and closing are suggested, with radii of thirty-two and eighty-six, respectively. Figure 5 illustrates the outcome of these concepts.

3.3. Thin Vessels Segmentation

The process of segmenting thin vessels involves two stages similar to those used for thick vessels, as outlined in figure 5. However, the specific methods are not elaborated upon in this section. Nevertheless, the PSO-HRVSO parameters for these shared stages will be outlined here.

Building upon the methodology described in the preceding section, and considering the finer scale of thin blood vessels which occupy smaller pixel sizes, a disk-shaped structuring element with radii of 5 and 25 pixels is PSO-HRVSO for opening and closing operations, respectively. As thin vessels encompass only a small percentage of the image, their total reflectance component value is comparatively lower than that of thick vessels. To enhance the visibility of these small white regions, a σ value of twenty is utilized to expand the cut-off regions of the filter. This enhancement improves all white components of the image, including the small vessels, albeit at the expense of thinning the thick and major veins of the vascular tree. However, this thinning effect will later be rectified by merging the segmented image of thick veins with the resultant image of subsequent steps.

When analyzing a gray-scale image in segments, the parts within it often resemble certain distribution curves. Two-dimensional matched filters are specifically crafted to amplify image sections that correspond to a particular distribution. Thus, this filtering technique seeks a level of correlation between the specified distribution and the local image area. The strategy behind employing a matched filtering method aims to identify segmented linear segments of blood vessels in fundus images. These segments' grayscale profile can typically be approximated by a Gaussian-shaped curve [62]. This Gaussian distribution, referred to as the kernel, undergoes rotation by an angular

step θ. Subsequently, it is convolved with the input image areas to enhance the matched regions. The rotation of the kernel is achieved through a rotation matrix RM, represented as follows:

$$RM = \begin{bmatrix} cos\theta & -sin\theta \\ sin\theta & cos\theta \end{bmatrix} \tag{23}$$

Non-vessel regions (i.e. low value of response) are not enhanced. The matched filter kernel is defined as follows:

$$f_{matched}(x,y) = -k\ exp\left(\frac{-x^2}{2\sigma^2}\right), for\ |y| \leq L/2 \tag{24}$$

Considerations should be made regarding the length (L) of the vessel's piecewise element and the spread (σ) of the kernel intensity profile. It is notable in the literature that blood vessels typically exhibit low curvatures. Therefore, it is crucial to search for rotations of anti-parallel pairs within estimated piecewise elements. Additionally, small blood vessels often lack significant local contrast. Despite previous homomorphic enhancement techniques, small vessels exhibit a low reflectance component compared to other inner surfaces of the human eye. Their appearance is characterized by lower illumination than the relative background, and their width decreases as they traverse the vascular tree.

To address these factors, vessel orientation may vary, and it is assumed that the vessel direction aligns with the y-axis. For thin vessel segmentation, the kernel undergoes rotation at seven-degree intervals, spanning angles from θ = 0, 7, 14 to 182 degrees, resulting in 26 different rotations. Recommended parameters for this methodology include a σ value of 0.8 and a kernel size of 7 × 7 pixels. This choice is informed by the common widths of retinal blood vessels, which typically range from 2 to 10 pixels (equivalent to 36 to 180μm). By employing this method, the likelihood of false detection of vasculature is reduced, consequently lowering the false positive rate.

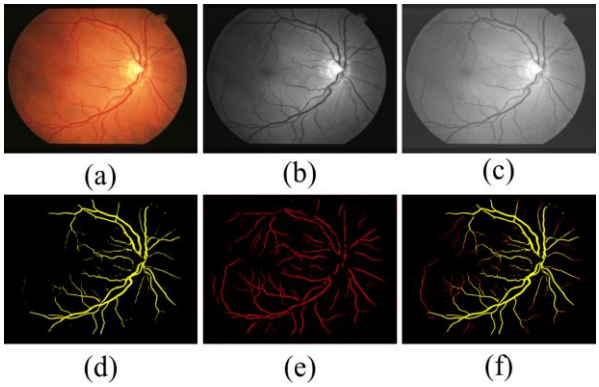

Figure 5: Vessels Segmentation: (a) Input RGB, (b) Green Component, (c) PSO Optimized, (d) Segmented Thick Vessels, (e) Segmented Thin Vessels, (f) Combined Vessels

3.4. Post Processing

The integration of thick and thin vessel segmentation in binary form involves applying a bitwise OR operation, followed by the generation of a final segmentation image illustrating the outcomes from both branches depicted in Figure 1. To eliminate small undesired components and noise generated in prior phases, a final post-processing step is executed. This step employs morphological image techniques including dilation, erosion, and a connectivity assessment to eliminate binary elements smaller than a predetermined pixel size, resulting in a definitive binary image for

subsequent evaluation. The ultimate outcome of the segmentation procedure is depicted in Figure 5(f).

4. RESULTS AND DISCUSSION

This section presents the performance outcomes of the PSO-HRVSO method applied to two eye fundus datasets for retinal vessel segmentation: DRIVE [51] and STARE [50], both publicly accessible. The DRIVE dataset comprises 40 images divided into two subsets of 20 elements each, designated as the training and test sets. All images were captured using a Canon CR5 nonmydriatic 3CCD camera with a 45^0 field of view and a spatial resolution of 565 × 584 pixels [91]. Additionally, the DRIVE image dataset includes manual segmentation conducted and validated by three trained human observers with medical expertise. The training subset involves the manual segmentation of one set by a single human observer, while the test subset underwent manual segmentation by two human observers, offering dual perspectives and establishing ground-truth images for performance analysis.

On the other hand, the STARE dataset comprises 397 digitized eye fundus images acquired using a TopCon TVR-50 fundus camera with a 35^0 field of view and a spatial resolution of 605×700 pixels [50]. Among these images, manual segmentation was performed for only 25 by two observers. The first observer segmented 11.2% of the entire image pixels as vascular tree pixels, while the second observer segmented a total of 14.6%. Both datasets encompass healthy and diseased fundus images, including various vascular abnormalities, diabetic retinopathy, choroidal neovascularization, arteriosclerotic retinopathy, among others.

To conduct a mathematical analysis and determine the accuracy of segmentation, three performance metrics are employed: Specificity (Spe), Sensitivity (Sen), and Accuracy (Acc). These metrics are defined mathematically as follows:

$$Sensitivity(Sen) = \frac{True\ Positive(T_P)}{True\ Positive(T_P) + False\ Negative(F_N)}$$

$$Specificity(Spe) = \frac{True\ Negative(T_N)}{True\ Negative(T_N) + False\ Positive(F_P)}$$

$$Accuracy(Acc) = \frac{T_P + T_N}{T_P + T_N + F_P + F_N}$$

Table 1: Results of the PSO-HRVSO methodology applied to DRIVE dataset

Images	Observer 1			Observer 2		
	Sen	Spe	Acc	Sen	Spe	Acc
01_test	0.8358	0.9742	0.9754	0.8437	0.9834	0.9715
02_test	0.8159	0.9867	0.9823	0.8164	0.9847	0.9794
03_test	0.8422	0.9831	0.9854	0.8519	0.9881	0.9837
04_test	0.7891	0.9928	0.9745	0.7974	0.9943	0.9829
05_test	0.7843	0.9936	0.9942	0.8036	0.9942	0.9918
06_test	0.8251	0.9849	0.9937	0.8284	0.9837	0.9916
07_test	0.8735	0.9874	0.9821	0.8734	0.9862	0.9864
08_test	0.8715	0.9942	0.9825	0.8839	0.9911	0.9838
09_test	0.8694	0.9837	0.9875	0.8734	0.9871	0.9827
10_test	0.8846	**0.9957**	0.9943	0.8858	0.9958	0.9918
11_test	0.8723	0.9943	0.9843	0.8868	0.9969	0.9837
12_test	0.8264	0.9785	0.9826	0.8234	0.9741	0.9784
13_test	0.8531	0.9938	0.9746	0.8519	0.9961	0.9721
14_test	0.8591	0.9892	0.9853	0.8587	0.9873	0.9864
15_test	0.8664	0.9875	0.9746	0.8738	0.9834	0.9766
16_test	0.8697	0.9828	0.9748	0.8769	0.9845	0.9784
17_test	0.8856	0.9914	0.9872	0.8821	0.9961	0.9867
18_test	**0.8946**	0.9849	0.9836	0.8937	0.9837	0.9817
19_test	0.8935	0.9932	0.9941	**0.8981**	0.9957	0.9969
20_test	0.8816	0.9941	0.9843	0.8776	**0.9971**	0.9792
21_test	0.8829	0.9852	0.9971	0.8872	0.9831	0.9944
22_test	0.8426	0.9847	0.9876	0.8265	0.9881	0.9848
23_test	0.8247	0.9911	**0.9982**	0.8319	0.9935	**0.9971**
24_test	0.8167	0.9927	0.9934	0.8264	0.9938	0.9964
25_test	0.8935	0.9857	0.9861	0.8897	0.9862	0.9908
Mean	0.8542	0.9882	0.9856	0.8577	0.9891	0.9852

True Positive (T_P) denotes the number of pixels identified as vessels in both the ground-truth and the segmented image. True Negative (T_N) indicates the count of pixels accurately classified as non-vessels in both the ground-truth and the segmented image. False Positive (F_P) represents the number of pixels identified as vessels in the segmented image but are non-vessel pixels in the ground-truth. Finally, False Negative (F_N) illustrates the number of pixels incorrectly classified as non-vessels in the segmented image when they correspond to vessels in the ground-truth.

Table 1 displays the performance results of applying segmentation metrics from the PSO-HRVSO methodology to the DRIVE dataset against observer 1 and observer 2. The method achieves a specificity of 0.9882, sensitivity of 0.8542, and average precision of 0.9856 compared to observer 1.

Similarly, against observer 2, the method achieves averages of 0.9891, 0.8577, and 0.9852 for these metrics, respectively. The maximum specificity values against observers 1 and 2 occur in image 10_test, reaching 0.9957 and in image 20_test, reaching 0.9971, respectively. Conversely, the minimum specificity values against observers 1 and 2 are 0.9742 and 0.9741, observed in images 01_test and 12_test, respectively.

Table 2 presents the metrics results of comparing the segmentation performed by the PSO-HRVSO method with both observers for the STARE data-set. The average sensitivity, specificity,

and accuracy achieved when comparing the segmented image with the ground-truth of observer 1 are 0.8577, 0.9868, and 0.9836, respectively. Similarly, when compared with the ground-truth of observer 2, these metrics are 0.8576, 0.9868, and 0.9831. The highest specificity values against observers 1 and 2 are 0.9974 in image im0038 and 0.9967 in image im0021, respectively. Conversely, the lowest specificity values against observers 1 and 2 are 0.9718 in image im0278 and 0.9739 in image im0056.

Table 2: Results of the PSO-HRVSO methodology applied to STARE dataset

Images	Observer 1			Observer 2		
	Sen	Spe	Acc	Sen	Spe	Acc
im0001	0.7925	0.9921	0.9951	0.7895	0.9878	0.9955
im0006	0.8244	0.9937	0.9927	0.8235	0.9938	0.9884
im0008	0.8257	0.9841	0.9842	0.8284	0.9926	0.9824
im0009	0.8317	0.9964	0.9934	0.8321	0.9897	**0.9968**
im0012	0.8341	0.9859	0.9763	0.8364	0.9918	0.9719
im0015	0.8347	0.9811	0.9748	0.8369	0.9792	0.9737
im0017	0.8522	0.9842	0.9822	0.8581	0.9846	0.9818
im0021	0.8761	0.9964	0.9851	0.8743	**0.9967**	0.9841
im0024	0.8795	0.9937	0.9837	0.8784	0.9896	0.9862
im0038	0.8628	**0.9974**	0.9942	0.8617	0.9933	0.9921
im0047	0.8748	0.9833	0.9901	0.8788	0.9818	0.9912
im0056	0.8691	0.9719	0.9871	0.8738	0.9739	0.9887
im0081	0.8824	0.9848	0.9833	0.8654	0.9864	0.9837
im0090	0.8857	0.9927	0.9858	0.8855	0.9899	0.9868
im0102	0.8749	0.9967	0.9869	0.8765	0.9927	0.9829
im0138	0.8869	0.9924	0.9925	0.8815	0.9964	0.9924
im0154	0.8871	0.9817	0.9847	0.8911	0.9791	0.9843
im0197	0.8215	0.9824	0.9723	0.8233	0.9867	0.9755
im0243	0.8166	0.9861	0.9611	0.8167	0.9865	0.9581
im0251	0.8546	0.9913	0.9637	0.8516	0.9922	0.9655
im0274	0.8612	0.9743	0.9728	0.8644	0.9854	0.9737
im0278	**0.8927**	0.9718	0.9738	**0.8917**	0.9739	0.9716
im0289	0.8715	0.9738	0.9829	0.8719	0.9718	0.9867
im0294	0.8657	0.9955	0.9954	0.8655	0.9897	0.9891
im0305	0.8852	0.9862	**0.9973**	0.8837	0.9857	0.9944
Mean	0.8577	0.9868	0.9836	0.8576	0.9868	0.9831

In Table 3, the results obtained are numerically contrasted against contemporary supervised and unsupervised methods, showcasing the efficiency and computational time across both datasets. Notably, the table highlights the highest average values among the three metrics for both supervised and unsupervised methods, which are denoted in bold. Specifically, in terms of specificity and accuracy, PSO-HRVSO attains the highest values of 0.9846 and 0.9856, respectively, whereas sensitivity peaks at 0.9230 with Liskowski et al. [64] for the DRIVE dataset. Similarly, for the STARE dataset, PSO-HRVSO achieves the highest specificity and accuracy scores of 0.9868 and 0.9833, while Liskowski et al. [64] secures the highest sensitivity at 0.9207. Despite not yielding the optimal outcomes, it's noteworthy that the approach is closely comparable in numerical terms

to methods necessitating training processes and ground-truth data, such as supervised methods, albeit with higher computational expenses.

Table 3: Comparative analysis of outcomes obtained from implementing the PSO-HRVSO methodology on both the DRIVE and STARE datasets, juxtaposed with state-of-the-art supervised and unsupervised methods.

Method	Year	DRIVE Dataset			STARE Dataset			Processing Time
		Sen	Spe	Acc	Sen	Spe	Acc	
Supervised methods								
Liskowski et al. [64]	2016	**0.9230**	0.9241	0.9160	**0.9207**	0.9304	0.9309	92.0s
Zhang et al. [65]	2017	0.7861	0.9712	0.9466	0.7882	0.9729	0.9547	23.40s
Orlando et al. [66]	2017	0.7897	0.9684	-	0.7680	0.9738	-	-
Dasgupta et al. [67]	2017	0.7691	0.9801	0.9533	-	-	-	-
Yan et al. [68]	2018	0.7653	0.9818	0.9542	0.7581	0.9846	0.9612	-
Thangaraj et al. [69]	2018	0.8014	0.9753	0.9606	0.8339	0.9536	0.9435	180.86s
Guo et al. [70]	2018	0.7046	0.9806	0.9613	0.5629	0.9816	0.9540	-
Yang et al. [71]	2019	0.756	0.9696	0.9421	0.7202	0.9733	0.9477	-
Jin et al. [72]	2019	0.7963	0.9800	0.9566	0.7595	0.9858	0.9641	17.65s
Cheng et al. [73]	2020	0.7672	0.9834	0.9559	-	-	-	-
Adapa et al. [74]	2020	0.6994	0.9811	0.9450	0.6298	0.9839	0.9486	81.0s
Wu et al. [75]	2020	0.7996	0.9813	0.9582	0.7963	0.9863	0.9672	88.0s
Unsupervised methods								
Zhang et al. [76]	2016	0.7743	0.9725	0.9476	0.7791	0.9758	0.9554	20.0s
Shahid et al. [77]	2017	0.7300	0.9790	0.9580	0.7900	0.9650	0.9510	-
Fan et al. [78]	2018	0.7360	0.9810	0.9610	0.7910	0.9710	0.9570	13.23s
Aguirre et al. [79]	2018	0.7854	-	0.9503	0.7116	0.9454	0.9231	-
Abdallah et al. [80]	2018	0.6887	0.9765	0.9389	0.6801	0.9711	0.9388	-
Pal et al. [81]	2018	0.6129	0.9744	0.9431	-	-	-	-
Yue et al. [82]	2018	0.7528	0.9731	0.9447	-	-	-	4.60s
Biswal et al. [83]	2018	0.7100	0.9700	0.9500	0.7000	0.9700	0.9500	3.30s
Diaz et al. [84]	2019	0.8464	0.9701	0.9619	0.8331	0.9619	0.9559	-
Wang et al. [85]	2019	0.7287	0.9775	0.9446	0.7526	0.9733	0.9503	4.50s
Roy et al. [86]	2019	0.4392	0.9622	0.9295	0.4317	0.9718	0.9488	0.10s
Zhou et al. [87]	2020	0.7262	0.9803	0.9475	0.7865	0.9730	0.9535	63.2s
Dos Santos et al. [88]	2020	0.7702	0.9695	0.9519	-	-	-	-
Shukla et al. [89]	2020	0.7015	0.9836	0.9476	0.7023	0.9863	0.9573	1.41s
Pachade et al. [90]	2020	0.7738	0.9721	0.9552	0.7769	0.9688	0.9543	4.78s
PSO-HRVSO	2024	0.8559	**0.9846**	**0.9854**	0.8577	**0.9868**	**0.9833**	24.0s

The mean processing times derived for each method as detailed in Table 3 were sourced from existing literature. Analysis of Table 3 reveals that the PSO-HRVSO method demonstrates shorter processing times compared to both supervised and unsupervised methods based on performance data. Furthermore, the PSO-HRVSO algorithm demonstrates competitive processing times compared to both supervised and unsupervised methods. Moreover, it exhibits superior efficiency values across all three-performance metrics.

5. PSEUDOCODE

Begin /* (Pseudocode) */

Begin /* (Gaussian Flitering over RGB Image) */
rgbImage = imread(Input RGB image.jpg'); */* Read the input RGB image */*
greenImage = rgbImage(:, :, 2); */*RGB to Green Component conversion */*
gaussianKarnel = Gaussian kernel size = 3;
σ = Standard Deviation
/ Compute the size of the Gaussian kernel based on the standard deviation */*
/ Calculate the Gaussian function for each pixel in the kernel */*

$$G(x,y) = (1 / (2 * \pi * sigma^2)) * exp(-((x^2 + y^2)/(2 * sigma^2)))$$

End /* (Gaussian Flitering over RGB Image) */

Begin /* *(Image Enhancement using PSO)* */
objectiveFunction = @(x) computeObjective(x, grayscaleImage); */* Define the objective function for image enhancement */*
numParticles = 100; */* Set PSO parameters */*
numIterations = 100;
maxVelocity = 2;
c1 = 2; */* Cognitive component weight */*
c2 = 2; */* Social component weight */*
/ Initialize particles and velocities */*
particlePositions = initializeParticles(numParticles);
particleVelocities = initializeVelocities(numParticles);
/ Initialize the best positions and global best position */*
particleBestPositions = particlePositions;
globalBestPosition = particlePositions(1, :);
/* Perform PSO iterations */
for iteration = 1:numIterations
particleFitness = evaluateFitness(objectiveFunction, particlePositions); */* Evaluate the fitness of each particle */*
for particle = 1:numParticles */* Update particle best positions */*
if particleFitness(particle) < evaluateFitness(objectiveFunction, particleBestPositions(particle, :))
particleBestPositions(particle, :) = particlePositions(particle, :);
end
end
[~, globalBestIndex]=min(particleFitness); */*Update global best position */*
globalBestPosition = particlePositions(globalBestIndex, :);
particleVelocities = updateVelocities(particleVelocities, particlePositions, particleBestPositions, globalBestPosition, c1, c2, maxVelocity); /* Update particle velocities and positions */
particlePositions = updatePositions(particlePositions, particleVelocities);
end
enhancedImage = performEnhancement(globalBestPosition, grayscaleImage); /* Perform image enhancement using the global best position */
End /* *(Image Enhancement using PSO)* */

Begin /* (Homomorphic Filtering) */

$$I(x,y) = luminance(x,y) * reflectance(x,y)$$

$$Z(x,y) = ln\big(I(x,y)\big) = ln\big(luminance(x,y) * reflectance(x,y)\big)$$
$$= ln\big(luminance(x,y)\big) + ln\big(reflectance(x,y)\big)$$

$$Fn[Z(x,y)] = Fn_z(u,v) + Fn_r(u,v)$$

$$H_{fn}(u,v) = 1 - exp\left(\frac{-D^2(u,v)}{2\sigma^2}\right)$$

$$G_{fn}(u,v) = Fn_z(u,v)H_{fn}(u,v) = Fn_l(u,v)H_{fn}(u,v) + Fn_r(u,v)H_{fn}(u,v)$$

$$Fn^{-1}\big[G_{fn}(u,v)\big] = Fn^{-1}\big[Fn_l(u,v)H_{fn}(u,v)\big] + Fn^{-1}\big[Fn_r(u,v)H_{fn}(u,v)\big]$$

$g(x,y) = luminance'(x,y) + reflectance'(x,y)$
$I'(x,y) = exp[g(x,y)] = exp[luminance'(x,y)]exp[reflectance'(x,y)]$
End /* (Homomorphic Filtering) */

Begin /* (Optimized Top-Hat Algorithm)
inputImage = enhancedImg; */* Read the input image */*
/ Apply morphological operations for noise removal or smoothing */*
SE = strel('disk', size); */* Define a disk-shaped structuring element with specified size */*
morphImage = imopen(grayImage, SE); */* Perform opening operation */*
tophatImage = imtophat(morphImage, SE); */* Perform TOP-HAT transform for image enhancement */*
End /* (Optimized Top-Hat Algorithm)
Thick_Threshold = median_filtering(tophatImage)
Thin_Threshold = matched_filtering(tophatImage)
Segmented_Vessels = Thick_Threshold + Thin_Threshold.

End /* (Pseudocode) */

6. CONCLUSION & FUTURE WORK

We introduce a novel approach aimed at enhancing the segmentation of the retinal vascular tree in human eye fundus images. The methodology hinges on a segmentation process divided into two branches: thin and thick vessel detection. Notably, our method achieves high specificity without necessitating manual segmentation or resource-intensive training techniques. Comparative analysis of our method, applied to both the DRIVE and STARE datasets, reveals its superiority over existing unsupervised methods in the literature. Particularly, it excels in extracting thin vessels with greater precision compared to current methodologies.

Central to our framework is the parameter variation of optimized top-hat and homomorphic filtering stages, tailored to the segmentation results of thin and thick vessels. This adaptive feature significantly enhances segmentation accuracy and specificity. However, a limitation of our proposal is its relatively lower sensitivity compared to state-of-the-art values. To address this, we plan to explore reinforced learning algorithms to optimize the methodology's parameters and improve sensitivity.

Looking ahead, we aim to integrate this method as a preprocessing step in a robust computer-aided diagnosis (CAD) system for classifying healthy and unhealthy fundus images based on retinal vessel segmentation. The crux lies in achieving high specificity segmentation, minimizing false positives, and ensuring accurate diagnostic interpretations—an aspect we prioritize in our proposal's development.

DECLARATION OF COMPETING INTEREST

The authors assert that they do not possess any identifiable competing financial interests or personal relationships that might have been perceived to impact the findings presented in this paper.

REFERENCES

[1] I.P. Chatziralli , E.D. Kanonidou , P. Keryttopoulos , P. Dimitriadis , L.E. Papazisis , The value of fundoscopy in general practice, The open ophthalmology journal 6 (2012) 4 .
[2] R. Vega , G. Sanchez-Ante , L.E. Falcon-Morales , H. Sossa , E. Guevara , Reti- nal vessel extraction using lattice neural networks with dendritic processing, Computers in biology and medicine 58 (2015) 20–30 .

[3] X. Xiao , S. Lian , Z. Luo , S. Li , Weighted res-unet for high-quality retina vessel segmentation, in: 2018 9th International Conference on Information Technol- ogy in Medicine and Education (ITME), IEEE, 2018, pp. 327–331 .

[4] J.J. Kanski , B. Bowling , Clinical ophthalmology: a systematic approach, Elsevier Health Sciences, 2011 .

[5] M. Ortega , M.G. Penedo , J. Rouco , N. Barreira , M.J. Carreira , Personal verifica- tion based on extraction and characterisation of retinal feature points, Journal of Visual Languages & Computing 20 (2) (2009) 80–90 .

[6] Y.Q. Zhao , X.H. Wang , X.F. Wang , F.Y. Shih , Retinal vessels segmentation based on level set and region growing, Pattern Recognition 47 (7) (2014) 2437–2446 .

[7] Y. Zhao , J. Xie , H. Zhang , Y. Zheng , Y. Zhao , H. Qi , Y. Zhao , P. Su , J. Liu , Y. Liu , Retinal vascular network topology reconstruction and artery/vein classifica- tion via dominant set clustering, IEEE transactions on medical imaging (2019) .

[8] Q. Li , B. Feng , L. Xie , P. Liang , H. Zhang , T. Wang , A cross-modality learn- ing approach for vessel segmentation in retinal images, IEEE transactions on medical imaging 35 (1) (2015) 109–118 .

[9] B. Yin , H. Li , B. Sheng , X. Hou , Y. Chen , W. Wu , P. Li , R. Shen , Y. Bao , W. Jia , Vessel extraction from non-fluorescein fundus images using orienta- tion-aware detector, Medical image analysis 26 (1) (2015) 232–242 .

[10] Y. Gavet , M. Fernandes , J. Debayle , J.-C. Pinoli , Dissimilarity criteria and their comparison for quantitative evaluation of image segmentation: applica- tion to human retina vessels, Machine vision and applications 25 (8) (2014) 1953–1966 .

[11] L.C. Neto , G.L. Ramalho , J.F.R. Neto , R.M. Veras , F.N. Medeiros , An unsupervised coarse-to-fine algorithm for blood vessel segmentation in fundus images, Ex- pert Systems with Applications 78 (2017) 182–192 .

[12] J.M. Patel , N.C. Gamit , A review on feature extraction techniques in con- tent based image retrieval, in: 2016 International Conference on Wireless Communications, Signal Processing and Networking (WiSPNET), IEEE, 2016, pp. 2259–2263 .

[13] M.M. Fraz , P. Remagnino , A. Hoppe , B. Uyyanonvara , A.R. Rudnicka , C.G. Owen , S.A. Barman , Blood vessel segmentation methodologies in retinal images–a survey, Computer methods and programs in biomedicine 108 (1) (2012) 407–433 .

[14] L. Mou , L. Chen , J. Cheng , Z. Gu , Y. Zhao , J. Liu , Dense dilated network with probability regularized walk for vessel detection, IEEE transactions on medi- cal imaging (2019) .

[15] R. Vaddi , M. Prabukumar , Comparative study of feature extraction techniques for hyper spectral remote sensing image classification: a survey, in: 2017 In- ternational Conference on Intelligent Computing and Control Systems (ICI- CCS), IEEE, 2017, pp. 543–548 .

[16] J. Mo , L. Zhang , Multi-level deep supervised networks for retinal vessel seg- mentation, International journal of computer assisted radiology and surgery 12 (12) (2017) 2181–2193.

[17] D. Liu , S. Wang , D. Huang , G. Deng , F. Zeng , H. Chen , Medical image classifica- tion using spatial adjacent histogram based on adaptive local binary patterns, Computers in biology and medicine 72 (2016) 185–200 .

[18] Y. Zhang , R. Liu , X. Wang , H. Chen , C. Li , Boosted binary harris hawks opti- mizer and feature selection, structure 25 (2020) 26 .

[19] R.A . Ibrahim , A .A . Ewees , D. Oliva , M. Abd Elaziz , S. Lu , Improved salp swarm algorithm based on particle swarm optimization for feature selection, Journal of Ambient Intelligence and Humanized Computing 10 (8) (2019) 3155–3169 .

[20] B.S. Vidya , E. Chandra , Entropy based local binary pattern (elbp) feature ex- traction technique of multimodal biometrics as defence mechanism for cloud storage, Alexandria Engineering Journal 58 (1) (2019) 103–114 .

[21] A .A . Ewees , M. Abd El Aziz , A.E. Hassanien , Chaotic multi-verse optimiz- er-based feature selection, Neural computing and applications 31 (4) (2019) 991–1006 .

[22] J. Sivic , A. Zisserman , Video google: A text retrieval approach to object match- ing in videos, in: null, IEEE, 2003, p. 1470 .

[23] M. Ahmad , S. Shabbir , D. Oliva , M. Mazzara , S. Distefano , Spatial-prior gener- alized fuzziness extreme learning machine autoencoder-based active learning for hyperspectral image classification, Optik 206 (2020) 163712 .

[24] H. Tang , Y. Xu , A. Lin , A.A. Heidari , M. Wang , H. Chen , Y. Luo , C. Li , Predicting green consumption behaviors of students using efficient firefly grey wolf-as- sisted k-nearest neighbor classifiers, IEEE Access 8 (2020) 35546–35562 .

[25] V. Nguyen , M. Blumenstein , An application of the 2d gaussian filter for enhancing feature extraction in off-line signature verification, in: 2011 In- ternational Conference on Document Analysis and Recognition, IEEE, 2011, pp. 339–343 .

[26] H. Chantar , M. Mafarja , H. Alsawalqah , A .A . Heidari , I. Aljarah , H. Faris , Fea- ture selection using binary grey wolf optimizer with elite-based crossover for arabic text classification, Neural Computing and Applications 32 (16) (2020) 12201–12220 .

[27] D.J. Reddy , T.A. Prasath , M.P. Rajasekaran , G. Vishnuvarthanan ,Brain and pan- creatic tumor classification based on glcm??k-nn approaches, in: Interna- tional Conference on Intelligent Computing and Applications, Springer, 2019, pp. 293–302 .

[28] B.A. Devi , M.P. Rajasekaran , Performance evaluation of mri pancreas image classification using artificial neural network (ann), in: Smart Intelligent Com- puting and Applications, Springer, 2019, pp. 671–681 .

[29] E. Rodríguez-Esparza , L.A. Zanella-Calzada , D. Oliva , M. Pérez-Cisneros , Au- tomatic detection and classification of abnormal tissues on digital mammo- grams based on a bag-of-visual-words approach, in: Medical Imaging 2020: Computer-Aided Diagnosis, 11314, International Society for Optics and Pho- tonics, 2020, p. 1131424 .

[30] Y. Hamamoto , S. Uchimura , M. Watanabe , T. Yasuda , Y. Mitani , S. Tomita , A ga- bor filter-based method for recognizing handwritten numerals, Pattern recog- nition 31 (4) (1998) 395–400 .

[31] A. Subudhi , M. Dash , S. Sabut , Automated segmentation and classification of brain stroke using expectation-maximization and random forest classifier, Biocybernetics and Biomedical Engineering 40 (1) (2020) 277–289 .

[32] Y. Zaychenko , G. Hamidov , Hybrid fuzzy cnn network in the problem of med- ical images classification and diagnostics, in: The International Conference on Natural Computation, Fuzzy Systems and Knowledge Discovery, Springer, 2019, pp. 883–891 .

[33] V. Aggarwal , A. Gupta , Integrating morphological edge detection and mu- tual information for nonrigid registration of medical images, Current Medical Imaging Reviews 15 (3) (2019) 292–300 .

[34] L. Nanni , S. Ghidoni , S. Brahnam , Handcrafted vs. non-handcrafted features for computer vision classification, Pattern Recognition 71 (2017) 158–172 .

[35] L. Satapathy , R. Tripathy , P. Das , A combination of variational mode decompo- sition and histogram equalization for image enhancement, National Academy Science Letters 42 (4) (2019) 333–336 .

[36] T. Jerman , F. Pernuš, B. Likar , Ž. Špiclin , Enhancement of vascular structures in 3d and 2d angiographic images, IEEE transactions on medical imaging 35 (9) (2016) 2107–2118 .

[37] J. Liu , J. Li , K. Zhang , U.A. Bhatti , Y. Ai , Zero-watermarking algorithm for medi- cal images based on dual-tree complex wavelet transform and discrete cosine transform, Journal of Medical Imaging and Health Informatics 9 (1) (2019) 188–194 .

[38] R.K. Meleppat , E.B. Miller , S.K. Manna , P. Zhang , E.N. Pugh Jr , R.J. Zawadzki , Multiscale hessian filtering for enhancement of oct angiography images, in: Ophthalmic Technologies XXIX, 10858, International Society for Optics and Photonics, 2019, p. 108581K .

[39] M. Raman , R. Korah , K. Tamilselvan , An automatic localization of optic disc in low resolution retinal images by modified directional matched filter., Int. Arab J. Inf. Technol. 16 (1) (2019) 1–7 .

[40] H. Andrea , I. Aranguren , D. Oliva , M. Abd Elaziz , E. Cuevas , Efficient im- age segmentation through 2d histograms and an improved owl search algorithm, International Journal of Machine Learning and Cybernetics (2020) 1–20 .

[41] G.R. Hernández , M.A. Navarro , N. Ortega-Sánchez , D. Oliva , M. Pérez-Cis- neros , Failure detection on electronic systems using thermal images and metaheuristic algorithms, IEEE Latin America Transactions 18 (08) (2020) 1371–1380 .

[42] S. Hinojosa , K.G. Dhal , M.A. Elaziz , D. Oliva , E. Cuevas , Entropy-based imagery segmentation for breast histology using the stochastic fractal search, Neuro- computing 321 (2018) 201–215 .

[43] M. Abd Elaziz , A .A . Ewees , D. Oliva , Hyper-heuristic method for multilevel thresholding image segmentation, Expert Systems with Applications 146 (2020) 113201 .

[44] F. Shaik , J. Chittemma , S.M. Islam , B.L. Reddy , S.D. Reddy , Enhancement of cerebral and retinal vascular structures using hessian based filters, in: ICCCE 2020, Springer, 2020, pp. 461–474 .

[45] T.M. Khan , M. Mehmood , S.S. Naqvi , M.F.U. Butt , A region growing and lo- cal adaptive thresholding-based optic disc detection, Plos one 15 (1) (2020) e0227566 .
[46] A. Rampun , B.W. Scotney , P.J. Morrow , H. Wang , J. Winder , Segmentation of breast mr images using a generalised 2d mathematical model with inflation and deflation forces of active contours, Artificial intelligence in medicine 97 (2019) 44–60 .
[47] E.R. Arce-Santana , A.R. Mejia-Rodriguez , E. Martinez-Peña , A. Alba , M. Mendez , E. Scalco , A. Mastropietro , G. Rizzo , A new probabilistic active contour region-based method for multiclass medical image segmentation, Medical & biological engineering & computing 57 (3) (2019) 565–576 .
[48] I. Aranguren , A. Valdivia , B. Morales-Castañeda , D. Oliva , M. Abd Elaziz , M. Perez-Cisneros , Improving the segmentation of magnetic resonance brain images using the lshade optimization algorithm, Biomedical Signal Processing and Control 64 (2021) 102259 .
[49] S. Chakraborty , S. Chatterjee , A. Das , K. Mali ,Penalized fuzzy c-means enabled hybrid region growing in segmenting medical images, in: Hybrid Machine In- telligence for Medical Image Analysis, Springer, 2020, pp. 41–65 .
[50] A. Hoover , V. Kouznetsova , M. Goldbaum , Locating blood vessels in retinal im- ages by piecewise threshold probing of a matched filter response, IEEE Trans- actions on Medical imaging 19 (3) (20 0 0) 203–210 .
[51] J. Staal , M.D. Abràmoff, M. Niemeijer , M.A. Viergever , B. Van Ginneken , Ridge-based vessel segmentation in color images of the retina, IEEE trans- actions on medical imaging 23 (4) (2004) 501–509 .
[52] Zhou C, Gao HB, Gao L: Particle swarm optimization (PSO) algorithm, Appl Res Comput, 20(12), 7-11, (2003).
[53] Li L, Li D: Applied PSO-RBF to aerial and satellite remote sensing image texture classification, Geomatics Inform. Sci.Wuhan Univ. 34(9): 1051-1054, (2009).
[54] M.S. Livingstone , D.H. Hubel , Psychophysical evidence for separate channels for the perception of form, color, movement, and depth, Journal of Neuro- science 7 (11) (1987) 3416–3468 .
[55] Marinakis Y, Iordanidou GR, Marinaki M: Particle swarm optimization for the vehicle routing problem with stochastic demands, Applied Soft Computing, 13(4): 1693-1704, (2013).
[56] J.V. Soares , J.J. Leandro , R.M. Cesar , H.F. Jelinek , M.J. Cree , Retinal vessel seg- mentation using the 2-d gabor wavelet and supervised classification, IEEE Transactions on medical Imaging 25 (9) (2006) 1214–1222 .
[57] P. Salembier , Comparison of some morphological segmentation algorithms based on contrast enhancement. application to automatic defect detection., in: 5. European Signal Processing Conference., 2, 1990, pp. 833–836 .
[58] A .M. Mendonca , A . Campilho , Segmentation of retinal blood vessels by com- bining the detection of centerlines and morphological reconstruction, IEEE transactions on medical imaging 25 (9) (2006) 1200–1213 .
[59] E.R. Dougherty , Mathematical morphology in image processing, Marcel Dekker, 1992 .
[60] A.V. Oppenheim , R.W. Schaffer , Digital Signal Processing, Prentice-Hall, 1975 .
[61] L.I. Voicu , H.R. Myler , A.R. Weeks , Practical considerations on color image enhancement using homomorphic filtering, Journal of Electronic Imaging 6 (1) (1997) 108–114 .
[62] S. Chaudhuri , S. Chatterjee , N. Katz , M. Nelson , M. Goldbaum , Detection of blood vessels in retinal images using two-dimensional matched filters, IEEE Transactions on medical imaging 8 (3) (1989) 263–269 .
[63] K. BahadarKhan , A .A . Khaliq , M. Shahid , A morphological hessian based ap- proach for retinal blood vessels segmentation and denoising using region based otsu thresholding, PloS one 11 (7) (2016) .
[64] P. Liskowski , K. Krawiec , Segmenting retinal blood vessels with deep neural networks, IEEE transactions on medical imaging 35 (11) (2016) 2369–2380 .
[65] J. Zhang , Y. Chen , E. Bekkers , M. Wang , B. Dashtbozorg , B.M. ter Haar Romeny , Retinal vessel delineation using a brain-inspired wavelet transform and ran- dom forest, Pattern Recognition 69 (2017) 107–123 .
[66] J.I. Orlando , E. Prokofyeva , M.B. Blaschko , A discriminatively trained fully con- nected conditional random field model for blood vessel segmentation in fun- dus images, IEEE transactions on Biomedical Engineering 64 (1) (2016) 16–27 .

[67] A. Dasgupta , S. Singh , A fully convolutional neural network based structured prediction approach towards the retinal vessel segmentation, in: 2017 IEEE 14th International Symposium on Biomedical Imaging (ISBI 2017), IEEE, 2017, pp. 248–251 .

[68] Z. Yan , X. Yang , K.-T. Cheng , Joint segment-level and pixel-wise losses for deep learning based retinal vessel segmentation, IEEE Transactions on Biomedical Engineering 65 (9) (2018) 1912–1923 .

[69] S. Thangaraj , V. Periyasamy , R. Balaji , Retinal vessel segmentation using neural network, IET Image Processing 12 (5) (2017) 669–678 .

[70] Y. Guo , Ü. Budak , A. ¸S engür , A novel retinal vessel detection approach based on multiple deep convolution neural networks, Computer methods and pro- grams in biomedicine 167 (2018) 43–48 .

[71] Y. Yang , F. Shao , Z. Fu , R. Fu , Discriminative dictionary learning for retinal ves- sel segmentation using fusion of multiple features, Signal, Image and Video Processing 13 (8) (2019) 1529–1537 .

[72] Q. Jin , Z. Meng , T.D. Pham , Q. Chen , L. Wei , R. Su , Dunet: A deformable net- work for retinal vessel segmentation, Knowledge-Based Systems 178 (2019) 149–162 .

[73] Y. Cheng , M. Ma , L. Zhang , C. Jin , L. Ma , Y. Zhou , Retinal blood vessel seg- mentation based on densely connected u-net, Mathematical Biosciences and Engineering 17 (4) (2020) 3088 .

[74] D. Adapa , A.N. Joseph Raj , S.N. Alisetti , Z. Zhuang , G. Naik , A supervised blood vessel segmentation technique for digital fundus images using zernike mo- ment based features, Plos one 15 (3) (2020) e0229831 .

[75] Y. Wu , Y. Xia , Y. Song , Y. Zhang , W. Cai , Nfn+: A novel network followed net- work for retinal vessel segmentation, Neural Networks (2020) .

[76] J. Zhang , B. Dashtbozorg , E. Bekkers , J.P. Pluim , R. Duits , B.M. ter Haar Romeny , Robust retinal vessel segmentation via locally adaptive derivative frames in orientation scores, IEEE transactions on medical imaging 35 (12) (2016) 2631–2644 .

[77] M. Shahid , I.A. Taj , Robust retinal vessel segmentation using vessel's loca- tion map and frangi enhancement filter, IET Image Processing 12 (4) (2018) 494–501 .

[78] Z. Fan , J. Lu , C. Wei , H. Huang , X. Cai , X. Chen , A hierarchical image matting model for blood vessel segmentation in fundus images, IEEE Transactions on Image Processing 28 (5) (2018) 2367–2377 .

[79] H. Aguirre-Ramos , J.G. Avina-Cervantes , I. Cruz-Aceves , J. Ruiz-Pinales , S. Ledesma , Blood vessel segmentation in retinal fundus images using gabor filters, fractional derivatives, and expectation maximization, Applied Mathe- matics and Computation 339 (2018) 568–587 .

[80] M.B. Abdallah , A.T. Azar , H. Guedri , J. Malek , H. Belmabrouk , Noise-estima- tion-based anisotropic diffusion approach for retinal blood vessel segmenta- tion, Neural Computing and Applications 29 (8) (2018) 159–180 .

[81] S. Pal , S. Chatterjee , D. Dey , S. Munshi , Morphological operations with itera- tive rotation of structuring elements for segmentation of retinal vessel struc- tures, Multidimensional Systems and Signal Processing 30 (1) (2019) 373–389 .

[82] K. Yue , B. Zou , Z. Chen , Q. Liu , Improved multi-scale line detection method for retinal blood vessel segmentation, IET Image Processing 12 (8) (2018) 1450–1457 .

[83] B. Biswal , T. Pooja , N.B. Subrahmanyam , Robust retinal blood vessel segmen- tation using line detectors with multiple masks, IET Image Processing 12 (3) (2017) 389–399 .

[84] D. Primitivo , R. Alma , C. Erik , V. Arturo , C. Edgar , P.-C. Marco , Z. Daniel , A hybrid method for blood vessel segmentation in images, Biocybernetics and Biomedical Engineering 39 (3) (2019) 814–824 .

[85] W. Wang , W. Wang , Z. Hu , Segmenting retinal vessels with revised top-bot- tom-hat transformation and flattening of minimum circumscribed ellipse, Medical & biological engineering & computing 57 (7) (2019) 1481–1496 .

[86] S. Roy , A. Mitra , S. Roy , S.K. Setua , Blood vessel segmentation of retinal image using clifford matched filter and clifford convolution, Multimedia Tools and Applications 78 (24) (2019) 34839–34865 .

[87] C. Zhou , X. Zhang , H. Chen , A new robust method for blood vessel segmen- tation in retinal fundus images based on weighted line detector and hidden markov model, Computer Methods and Programs in Biomedicine 187 (2020) 105231 .

[88] J.C.M. dos Santos , G.A. Carrijo , C.d.F. dos Santos Cardoso , J.C. Ferreira , P.M. Sousa , A.C. Patrocínio , Fundus image quality enhancement for blood ves- sel detection via a neural network using clahe and wiener filter, Research on Biomedical Engineering (2020) 1–13 .

[89] A.K. Shukla , R.K. Pandey , R.B. Pachori , A fractional filter based efficient algo- rithm for retinal blood vessel segmentation, Biomedical Signal Processing and Control 59 (2020) 101883 .

[90] S. Pachade , P. Porwal , M. Kokare , L. Giancardo , F. Meriaudeau , Retinal vascu- lature segmentation and measurement framework for color fundus and slo images, Biocybernetics and Biomedical Engineering (2020) .

[91] M. Niemeijer , J. Staal , B. van Ginneken , M. Loog , M.D. Abramoff, Compara- tive study of retinal vessel segmentation methods on a new publicly avail- able database, in: Medical imaging 2004: image processing, 5370, Interna- tional Society for Optics and Photonics, 2004, pp. 648–656 .